2024 IEEE/RSJ International Conference on Intelligent Robots and Systems (IROS)
October 14-18, 2024. Abu Dhabi, UAE

Towards Electricity-free Pneumatic Miniature Rotation Actuator for Optical Coherence Tomography Endoscopy

Tinghua Zhang[1,†], Sishen Yuan[2,†], Chao Xu[1,†], Peng Liu[1], Hongliang Ren[2,*] and Wu Yuan[1,*]

***Abstract*— Miniature rotation actuators have been extensively developed and utilized in optical coherence tomography (OCT) endoscopy, enabling distortion-free OCT imaging in complex and tortuous environments. However, the use of electrical-driven rotation actuators raises safety concerns. Although magnetic-driven rotation actuators have been reported in OCT endoscopy, their use can potentially interfere with other medical devices in clinical settings. Here, we propose a pneumatic miniature rotation actuator that eliminates the electricity and magnetism concerns in circumferential imaging for OCT endoscopy. The rotor of the actuator is designed as a windmill, enabling it to convert air energy into rotation energy. In addition, to maintain the stable rotation, both a sliding bearing with two supporting points and a glass spindle with a half-ball end surface are developed. The rotation speed of our pneumatic actuator can be controlled from 66 to 97 revolutions per second by adjusting the airflow rate from 3.25 to 4.00 liters per minute. By OCT imaging of the human fingers, we demonstrate the feasibility of the pneumatic actuator in electricity-free distal scanning OCT endoscopy. Our pneumatic rotation actuator has wide-ranging potential in various fiber-imaging modalities, including not only OCT but also ultrasound imaging that requires similar rotation capabilities.**

I. Introduction

Endoscopic optical coherence tomography (OCT) is a non-invasive, non-label, and high-resolution imaging technology for in vivo visualization of internal luminal organs [1]–[5]. It has been demonstrated for a wide range of clinical applications such as disease diagnosis and screening where traditional biopsy suffers from sampling error or risk of complications [6]–[10]. As a prime example, intravascular OCT offers high-resolution diagnostic images during percutaneous coronary intervention, resulting in improved clinical outcomes [11].

Currently, there are two methods, namely proximal scanning [2] and distal scanning [12], that enable OCT endoscopes to achieve circumferential imaging in internal luminal organs. Proximal scanning OCT endoscopy is achieved by employing a rotation mechanism near the proximal end of the OCT imaging probe to drive the distal circumferential scanning of the probe through a torque coil. However, this approach is susceptible to the nonuniform rotation of torque coil in tortuous lumens, such as cardiovascular and bronchi, resulting in distortions in OCT images [13], [14]. In contrast, the distal scanning OCT endoscopy has better stability in the circumferential scanning for tortuous environments due to the miniature rotation mechanism directly installed on the distal end of the imaging probe [15].

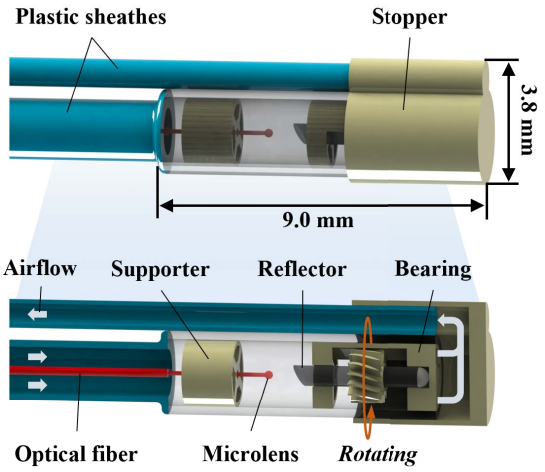

Fig. 1. Schematic of OCT imaging probe based on pneumatic miniature rotation actuator.

In recent years, interest has increased significantly in the development of miniature rotation mechanisms to achieve the distal circumferential scanning of OCT probes [16]. For example, Wang, *et al*. proposed a high-speed synchronous micromotor for intravascular OCT imaging [17]. Furthermore, a miniature piezoelectric-driven rotation actuator was designed to conduct distortion-free OCT imaging in tortuous vessels [14]. However, these designs raise the safety concern of electrical aspects, which hinders their practical application in clinical settings. To address the safety concern, Wang, *et al*. introduced a solution by developing a miniature rotator that utilizes an externally-actuated small magnet. However, the magnetic-driven actuator is susceptible to variations in distance between the external driver and the driven miniature magnet [18]–[21]. Additionally, magnetic systems can interfere with other medical devices in clinical settings, such as magnetic resonance imaging (MRI).

Here, we propose a pneumatic miniature rotation actuator

This work is supported in part by the Research Grants Council (RGC) of Hong Kong SAR (ECS24211020, GRF14203821, GRF14216222), the Innovation and Technology Fund (ITF) of Hong Kong SAR (ITS/240/21), the Science, Technology and Innovation Commission (STIC) of Shenzhen Municipality (SGDX20220530111005039), the Hong Kong Research Grants Council (RGC) Collaborative Research Fund (CRF C4026-21GF), the General Research Fund (GRF 14203323, GRF 14216022), the Research Impact Fund (RIF R4020-22), and the NSFC/RGC Joint Research Scheme N_CUHK420/22.

[1]Department of Biomedical Engineering, The Chinese University of Hong Kong, Hong Kong.

[2]Department of Electronic Engineering, The Chinese University of Hong Kong, Hong Kong.

*Corresponding author: Hongliang Ren, mail: hlren@ieee.org; Wu Yuan, mail: wyuan@cuhk.edu.hk.

†Equal contribution authors: Tinghua Zhang, Sishen Yuan, and Chao Xu.

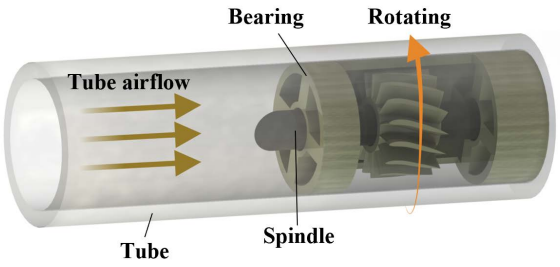

Fig. 2. Schematic of pneumatic miniature rotation actuator.

to perform electricity-free distal circumferential scanning in OCT endoscopy. As shown in Fig. 1, the rotor of the pneumatic actuator is designed as a windmill driven by the tube airflow inspired by the mechanism of the wind turbine. To ensure rotational stability, we fabricate a glass spindle with a half-sphere at one end to minimize friction. Meanwhile, another end of the spindle is designed as a reflector for OCT endoscopy. A sliding bearing with two supports is incorporated to reduce vibrations. The circumferential scanning speed of an OCT probe based on our pneumatic actuator can be controlled at the range of 66 to 97 revolutions per second (rps) by regulating the airflow rate. Moreover, the speed fluctuation is less than 1.3% by bending and swaying the OCT probe to mimic the turns and motions of luminal organs. To verify the feasibility of our pneumatic actuator in OCT endoscopy, we conduct high-resolution OCT imaging of the human finger. The results demonstrate that the pneumatic rotation actuator has excellent potential to replace the electric-driven distal scanning mechanism for stable circumferential imaging without safety concerns of electricity in OCT endoscopy.

The rest of this paper is organized as follows. Section II introduces the design of the miniature pneumatic actuator and corresponding OCT imaging probe. The experimental results, including rotation speed test and human finger imaging, are described in Section III. Finally, the paper is concluded in Section IV.

II. Design

A. Pneumatic Actuator Design

The pneumatic miniature actuator consists of a rotor, a spindle, a bearing and a tube, as shown in Fig. 2. The actuator is activated by using the tube airflow to drive the rotor. To efficiently convert wind energy into rotational energy, the rotor is designed in the form of a windmill. The wind energy (P) can be expressed as a sum of its kinetic energy [22]:

$$P = \frac{1}{2}\rho A v^3 , \tag{1}$$

where ρ is the air density, A is the area swept by the rotor and v is the air velocity. The rotational energy (P_m) can be determined by [23]

$$P_m = \frac{1}{2} C_P \rho A v^3 , \tag{2}$$

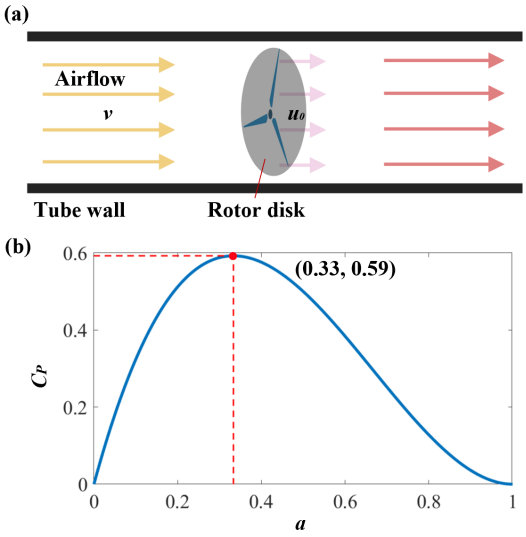

Fig. 3. (a) Disk model of energy conversion between wind energy and rotational energy of the windmill. (b) Theoretical power coefficient C_P versus axial interference factor a.

where C_P is the energy coefficient determined mainly by blade profile (cross-section of a blade) and blade number. Utilizing the one-dimensional momentum model [24], the rotor can be simplified as a disk in a tube, as shown in Fig. 3(a). Therefore, the energy coefficient is given by [25]

$$C_P = 4a(1-a)^2 , \tag{3}$$

where $a = 1 - u_0/v$ is called the axial interference factor, and u_0 indicates the axial velocity in the rotor disk. As shown in Fig. 3(b), the maximum convertible energy ($C_{P,max} \approx 0.59$ where $a \approx 0.33$) is calculated by differentiating the energy coefficient C_P with respect to the axial interference factor a, that is, up to 59% of the kinetic energy converted in a fluid tube can be obtained to useful work by the rotor disk.

1) Rotor: To achieve optimal rotation performance, the rotor is specifically designed with a focus on the blade profile and number. A typical profile (USA 25 AIRFOIL, see Fig. 4(a)) is employed to further determine its angle of attack (α) and fabricate the rotor (see Fig. 4(b)). As shown in Fig. 4(a), the wind force acting on the blade profile can be decomposed as the lift force (l) and drag force (d). Generally, lift and drag coefficients (Cl and Cd) are defined as [26]

$$Cl(\alpha, Re) = \frac{l}{\frac{1}{2}\rho v^2 c} , \tag{4}$$

$$Cd(\alpha, Re) = \frac{d}{\frac{1}{2}\rho v^2 c} , \tag{5}$$

where Re is the Reynolds number based on the chord length (c) and the air velocity as follows

$$Re = \frac{cv}{u} , \tag{6}$$

where u is the kinematic viscosity. C_l and C_d are functions of α, c, u and v. The angle of attack can be optimized by reasonably assuming other parameters to achieve desirable

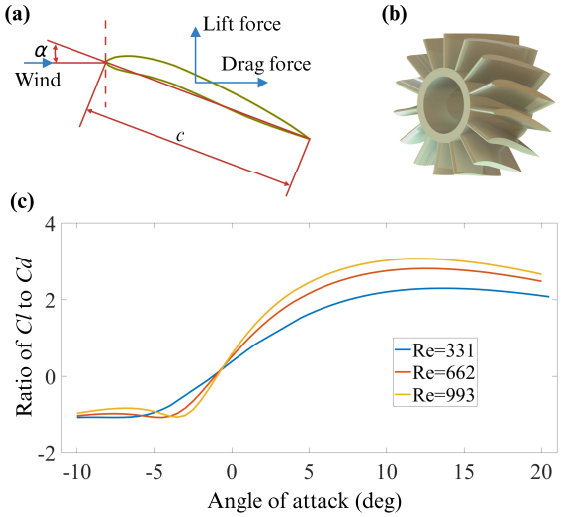

Fig. 4. Optimization of the rotor. (a) Static analysis of USA 25 AIRFOIL. (b) A rotor prototype based on USA 25 AIRFOIL. (c) Ratios of Cl to Cd versus the angle of attack with a fixed chord length of 1 mm at 331, 662, and 993 Reynolds numbers. Three Reynolds numbers correspond to 5-m/s, 10-m/s, and 15-m/s wind velocities at 1.5111E-5-m^2/s kinematic viscosity and 20 °C, respectively.

energy conversion, i.e., a maximum ratio of Cl to Cd.

Here, the curves of ratios of Cl to Cd versus the angle of attack are plotted at three Reynolds numbers in QBlade by assuming 1.5111E-5-m^2/s kinematic viscosity of air and 20 °C and fixing the 1-mm chord length, as shown in Fig. 4(c). Therefore, the 12-degree attack angle is determined, corresponding to an optimized ratio of Cl to Cd. In addition, the blade number is determined as 15 because the wind energy coefficient is extremely close to the theoretical maximum value under this condition [27]. While increasing the blade number would further approach the theoretical maximum value of the windmill's wind energy coefficient, it would also increase the fabrication difficulty. Finally, the length and diameter of the rotor are determined as 1.0 mm and 1.6 mm, respectively.

2) Spindle: Given that the actuator is used in OCT endoscopy, the spindle's design serves a dual purpose. It is not only responsible for maintaining the rotor's rotation but also functions as a reflector. To begin with, a cylindrical glass rod with dimensions of 0.6 mm in diameter and 4.0 mm in length is utilized as a blank for the spindle. The smooth surface of the rod helps minimize friction during rotation. Then, a 53-degree tilted plane is cut and is coated with 5-nm Cr, 100-nm Ag, and 100-nm TiO_2 by EB-600, Innovative Vacuum Solution Co., Ltd., generating a reflector with a reflectivity of about 91%. Finally, a half ball is fabricated at another end of the rod by curing a drop of ultraviolet (UV) glue, as shown in Fig. 5(a). The production of the hall ball is dependent on the surface tension of the UV glue. When a small drop of glue is placed on the 0-degree plane, it naturally forms a half-ball shape. As a result, the half ball has low friction in contact with the sliding bearing due to the low roughness of the cured glue.

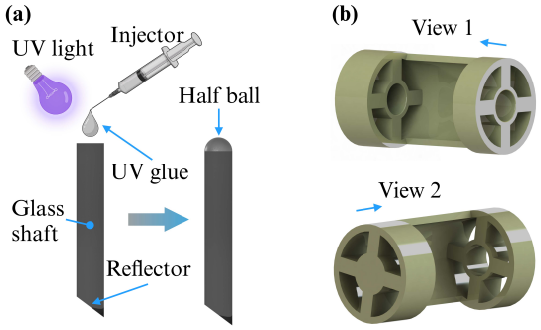

Fig. 5. Spindle and bearing designs. (a) Fabrication procedure of the spindle. (b) Drawings of the bearing from two perspectives.

3) Bearing: The bearing is utilized to ensure the smooth rotation of the spindle along with the rotor. Due to the challenges in fabricating a rolling bearing in a small size, we have chosen to utilize a sliding bearing instead. Furthermore, utilizing only one bearing to support the spindle results in a cantilever beam structure, leading to unstable rotation. To address the issue of unstable rotation, a one-piece, two-support sliding bearing is designed, as shown in Fig. 5(b). The diameter of the supports is 0.64 mm, providing a gap for the sliding rotation of the spindle. One of the supports is designed as a through hole, allowing the spindle to pass through. Another support is specifically designed to restrict the movement of the spindle. Other through-holes are reserved for the passage of airflow. To accommodate the rotor, the bearing is designed with an outer diameter of 2.0 mm and a length of 3.5 mm.

B. OCT Probe Design Based on Pneumatic Actuator

To ensure the safety of our pneumatic rotation in endoscopic OCT, we prioritize the transportation of the airflow and address any potential gas leakage concerns. As shown in Fig. 1, the airflow is generated by an external air source and pumped through the large plastic sheath. Then, it is directed away from the small plastic sheath by changing the airflow direction using the stopper. All connections are sealed with the UV glue. In addition, the tube of the pneumatic actuator, obtained by cutting off a section of transparent glass tube (outer diameter: 2.5 mm; inner diameter: 2.0 mm), is used as the OCT imaging window. To ensure the dexterity of the OCT endoscope in lumens, the tube's length is determined to be 8 mm.

To provide sufficient space for airflow passage, the laser beam for OCT endoscopy is transmitted by a single-mode fiber (SMF). The fiber is spliced with a short piece of coreless fiber (CLF) as a beam expander with a ball lens. To maintain coaxial alignment between the ball lens and the reflector during rotation, a supporter with a length of 1.5 mm is fabricated to secure the fiber in place. There are three steps related to the fiber fabrication process, as shown in Fig. 6. The CLF is first fusion-spliced to the SMF, and then precisely cleaved to a predefined length under a microscope. Finally, the ball lens of fiber is formed at the distal end of the CLF by employing an electric arc fusion splicer.

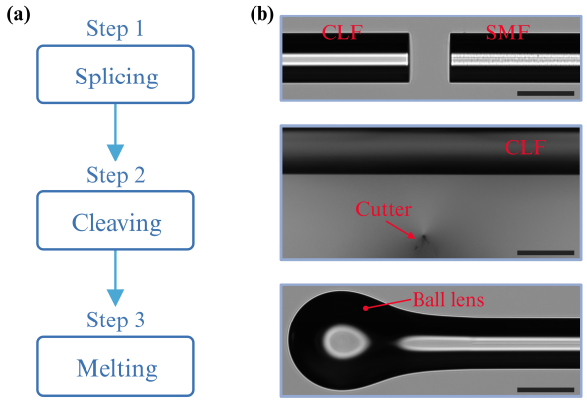

Fig. 6. Fabrication procedure. (a) Flow chart for the fabrication of a fiber with ball lens. (b) Representative photographs corresponding to each fabrication step of (a). All scale bars are 125 μm.

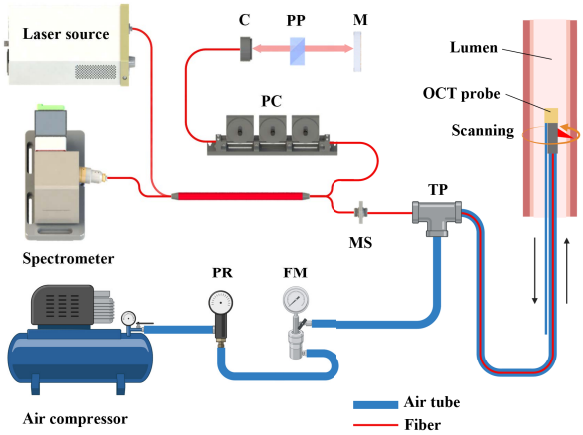

Fig. 7. Schematic of endoscopy system based on the proposed pneumatic actuator. C achromatic collimator, M mirror, PC polarization controller, PP prism pair, MS mating sleeve, TP tee pipe, PR pressure regulator, FM flow meter.

III. Experiments

To characterize the rotation performances of our pneumatic actuator and validate its application feasibility in OCT endoscopy, an OCT endoscopy system is constructed, as shown in Fig. 7. It includes an OCT engine, a pneumatic unit, and an OCT imaging probe based on our pneumatic actuator. The rotor and the sliding bearing of the pneumatic actuator are manufactured by a three-dimensional printer with the printing resolution of ±20 μm (Micro X115, Jiangmen Xingsheng Technology Co., Ltd.).

We employ a spectral domain OCT engine to generate cross-sectional images of tissue [28]. It consists of a light source (centre wavelength: 842 nm; 3-dB bandwidth: about 160 nm) (MT-850-HP, Superlum Diodes Ltd., Ireland), an ultra-broadband 50:50 fiber coupler (TW850R5A2, Thorlabs, USA), and an ultra-high speed spectrometer (Cobra-S 800, Wasatch Photonics Inc., USA), which can operate at bandwidth 650 - 950 nm and achieve maximum 250-kHz scanning rate. The reference arm comprises a prism pair, a reflective mirror, and a fiber port collimator (PAF2-A7B, Thorlabs, USA). Unlike the proximal scanning mechanism to drive the OCT imaging probe for circumferential tissue image acquisition, the OCT probe based on the proposed actuator is directly connected to the coupler port of the sample arm by a mating sleeve.

The pneumatic unit, comprising an air compressor (storage capacity: 30 L; maximum exhaust volume: 120 L/min; maximum pressure: 0.8 MPa) and a pressure regulator (ITV2050-312L, SMC), is utilized to drive the proposed actuator. The airflow rate is regulated by adjusting the flow meter (MF-4003, LANGFAN) to control the rotation speed of the proposed actuator. The tee pipe (inner diameter: 2 mm; outer diameter: 4.5 mm) is used to connect the fiber and air tube.

A. Characterization of Pneumatic Actuator

According to equation (2), the rotation speed of the pneumatic actuator can be controlled by regulating the airflow velocity, that is, adjusting the airflow rate can control the rotation speed in the tube because of

$$v = \frac{q}{S}, \tag{7}$$

where q is the airflow rate and S is the cross-sectional area of the tube. Using a laser detector, the rotation speed of our pneumatic actuator is measured by calculating the time of each revolution.

First, the OCT probe is stretched as shown in Fig. 8(a). In the condition, the rotation speeds are measured at flow rates of 4.00 L/min, 3.50 L/min and 3.25 L/min. The measurement results demonstrate that the rotation speed increases with the flow rate, and it can be controlled from 66 rps to 97 rps by regulating the flow rate from 3.25 L/min to 4.00 L/min. To further evaluate the rotational stability of pneumatic actuator, we measure the rotation speed by bending and swaying the OCT imaging probe to mimic the turns and motions of luminal organs, as shown in Fig. 8(b) and (c). Under the conditions of bending angles of 30°, 60°, and 90° with an airflow rate of 4.00 L/min, there are no significant fluctuations in rotation speed. Compared to the stretching condition, the fluctuation is within 1.3%. Under the conditions of swaying frequencies of 60 Hz, 90 Hz, and 120 Hz with the airflow rate of 4.00 L/min, there are also no significant fluctuations in speed again. The fluctuation is within 0.9% compared to the frequency of 0 Hz. Under the above conditions, the speed fluctuations for five minutes are less than 7%, which is comparable with the electrically driven motor [17]. We believe that speed stabilization is influenced by two factors. Firstly, the shell of our pneumatic actuator is a rigid part, which ensures the stability of airflow through the rotor. Secondly, the integrated design of the sliding bearing provides the condition of stable rotation. The experimental results demonstrate that our pneumatic actuator's rotation speed can be controlled and remains stable, making it suitable for application in distal scanning OCT endoscopy.

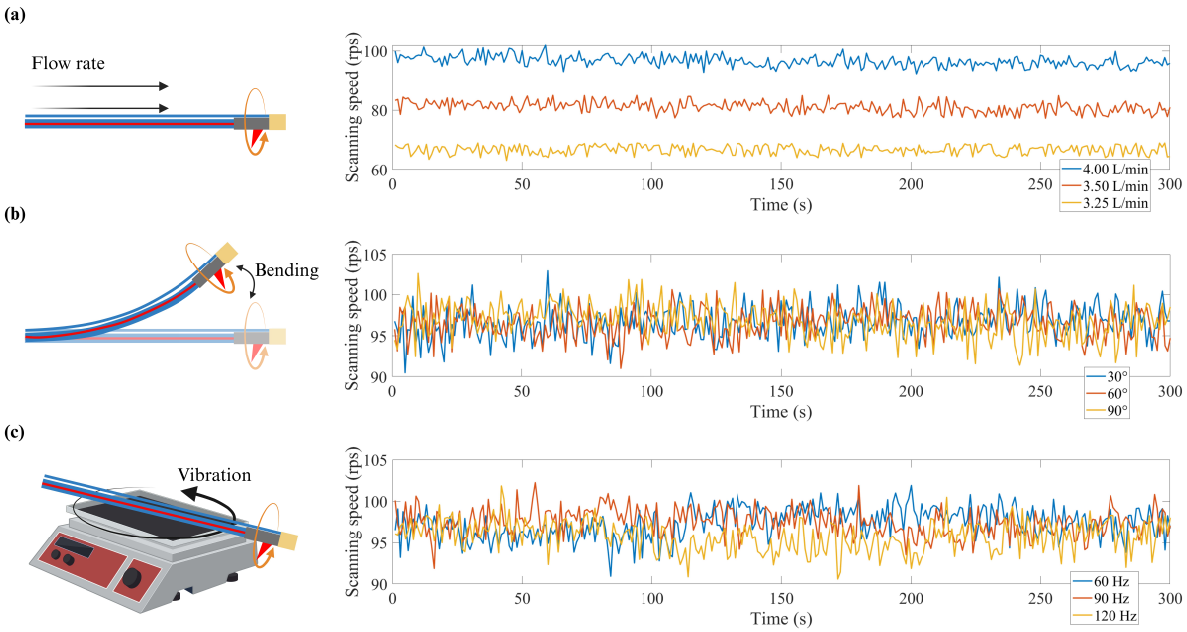

Fig. 8. Characterisation of rotation performance of the proposed pneumatic actuator. (a)-(c) The left figure represents the schematic of rotation speed test. The right figure shows the rotation speed of each second for five minutes corresponding to the three conditions of the left setup. The reflection laser is detected by a laser sensor, allowing the computation of scanning speed by measuring the time taken for each revolution of the laser beam. The laser sensor and acquisition card for the scanning speed measurement are PDA36A2, THORLABS, and NI USB-6210 (250 kHz), respectively.

B. Validation of OCT Endoscopy

To validate the feasibility of our pneumatic actuator in distal scanning OCT endoscopy, we conducted the OCT endoscopy experiment for the human finger, as shown in Fig. 9. First, we carry out the optical design to obtain a desired working distance (W), as shown in Fig. 9(a). Here, the ball lens is assumed to be spherical, and the refraction on the wall of the glass tube is ignored. There are four design parameters: the length of the CLF (S), the diameter of the ball lens (D), the radius of the glass tube (R), and the distance between the ball lens and the reflector (B). To find the conditions under which an optimal resolution can be achieved for a desired working distance with a given ball lens diameter (250 μm), ray-tracing simulations are carried out with Zemax (Zemax, LLC.) by assuming a uniform pure silica index profile in both the beam expander and ball lens. The simulation results show that when the length of the CLF is 195 μm, an optimal focused length of the laser beam (B+(R+W)/sin74°) is 2386 μm, that is, the laser beam can focus at approximately 274 μm outside the glass tube.

Then, the OCT imaging probe driven by our pneumatic actuator is wrapped by two human fingers, as shown in Fig. 9 (b). The OCT imaging probe circumferentially scans the fingers at the rotation speed of 66 rps. By matching the sampling frequency and the circumferential scanning speed, the OCT image of the human fingers is captured as shown in Fig. 9(c). The finger's layer structure, including the external fingerprint, internal fingerprint, epidermis, and dermis, is clearly observed. This demonstrates the successful application of our pneumatic actuator in endoscopic OCT imaging.

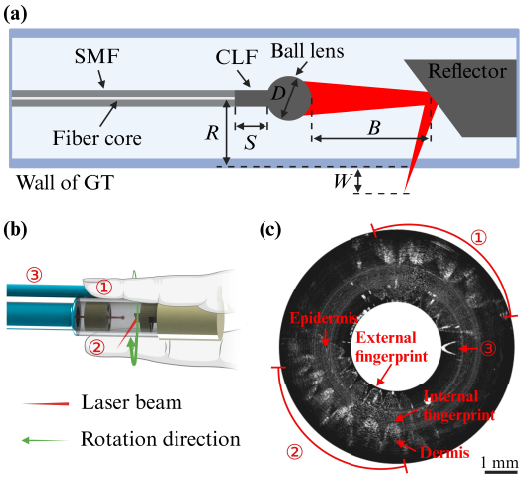

Fig. 9. OCT endoscopy for the human finger using the proposed pneumatic rotation actuator. (a) Working distance design of OCT imaging probe. (b) OCT endoscopy schematic. (c) Representative OCT image of the human finger.

IV. Conclusions

This paper proposes a pneumatic miniature rotation actuator that features stable rotation. The rotation speed of the pneumatic actuator can be controlled from 66 to 97 rps by regulating the airflow rate from 3.25 to 4.00 L/min. By in vitro OCT imaging of the human fingers, we demonstrate the actuator's feasibility in electricity-free distal scanning OCT endoscopy. Our pneumatic rotation actuator provides an electricity-free scanning method for OCT endoscopy and has significant potential in the application of other imaging

modalities, such as endoscopic ultrasound. However, our pneumatic actuator is still in its infancy, and several aspects require enhancement in its design and functionality for future clinical translation. First, it is necessary to conduct clinical evaluations further for our pneumatic actuator in vasculature and bronchi. Secondly, the windmill rotor could be optimized to enhance energy conversion efficiency, increasing the maximum rotation speed. Finally, the structure of the rotation actuator should be improved to reduce its outer diameter, so that it can be used in narrower luminal organs [29].

REFERENCES

[1] G. J. Tearney, M. E. Brezinski, B. E. Bouma, S. A. Boppart, C. Pitris, J. F. Southern, and J. G. Fujimoto, "In vivo endoscopic optical biopsy with optical coherence tomography," *Science*, vol. 276, no. 5321, pp. 2037–2039, 1997.

[2] W. Yuan, J. Mavadia-Shukla, J. Xi, W. Liang, X. Yu, S. Yu, and X. Li, "Optimal operational conditions for supercontinuum-based ultrahigh-resolution endoscopic oct imaging," *Optics letters*, vol. 41, no. 2, pp. 250–253, 2016.

[3] W. Yuan, R. Brown, W. Mitzner, L. Yarmus, and X. Li, "Super-achromatic monolithic microprobe for ultrahigh-resolution endoscopic optical coherence tomography at 800 nm," *Nature communications*, vol. 8, no. 1, p. 1531, 2017.

[4] C. Xu, T. Zhang, P. Liu, and W. Yuan, "Miniature ultrahigh-resolution visible-light oct endoscopy," in *Endoscopic Microscopy XIX*, vol. 12820. SPIE, 2024, pp. 32–35.

[5] C. Xu, Z. Fang, T. Zhang, H. Gao, T. Zhang, P. Liu, H. Ren, and W. Yuan, "Submillimeter robotic oct neuroendoscope for deep-brain imaging in vivo," in *Advanced Biomedical and Clinical Diagnostic and Surgical Guidance Systems XXII*, vol. 12831. SPIE, 2024, pp. 5–8.

[6] M. E. Brezinski, G. J. Tearney, B. E. Bouma, J. A. Izatt, M. R. Hee, E. A. Swanson, J. F. Southern, and J. G. Fujimoto, "Optical coherence tomography for optical biopsy: properties and demonstration of vascular pathology," *Circulation*, vol. 93, no. 6, pp. 1206–1213, 1996.

[7] M. J. Gora, J. S. Sauk, R. W. Carruth, K. A. Gallagher, M. J. Suter, N. S. Nishioka, L. E. Kava, M. Rosenberg, B. E. Bouma, and G. J. Tearney, "Tethered capsule endomicroscopy enables less invasive imaging of gastrointestinal tract microstructure," *Nature medicine*, vol. 19, no. 2, pp. 238–240, 2013.

[8] W. Yuan, C. Kut, W. Liang, and X. Li, "Robust and fast characterization of oct-based optical attenuation using a novel frequency-domain algorithm for brain cancer detection," *Scientific reports*, vol. 7, no. 1, p. 44909, 2017.

[9] W. Yuan, D. Chen, R. Sarabia-Estrada, H. Guerrero-Cázares, D. Li, A. Quiñones-Hinojosa, and X. Li, "Theranostic oct microneedle for fast ultrahigh-resolution deep-brain imaging and efficient laser ablation in vivo," *Science advances*, vol. 6, no. 15, p. eaaz9664, 2020.

[10] W. Yuan, J. Thiboutot, H.-c. Park, A. Li, J. Loube, W. Mitzner, L. Yarmus, R. H. Brown, and X. Li, "Direct visualization and quantitative imaging of small airway anatomy using deep learning assisted diffractive oct," *IEEE Transactions on Biomedical Engineering*, vol. 70, no. 1, pp. 238–246, 2022.

[11] G. J. Tearney, E. Regar, T. Akasaka, T. Adriaenssens, P. Barlis, H. G. Bezerra, B. Bouma, N. Bruining, J.-m. Cho, S. Chowdhary *et al.*, "Consensus standards for acquisition, measurement, and reporting of intravascular optical coherence tomography studies: a report from the international working group for intravascular optical coherence tomography standardization and validation," *Journal of the American College of Cardiology*, vol. 59, no. 12, pp. 1058–1072, 2012.

[12] P. H. Tran, D. S. Mukai, M. Brenner, and Z. Chen, "In vivo endoscopic optical coherence tomography by use of a rotational microelectromechanical system probe," *Optics letters*, vol. 29, no. 11, pp. 1236–1238, 2004.

[13] N. Uribe-Patarroyo and B. E. Bouma, "Rotational distortion correction in endoscopic optical coherence tomography based on speckle decorrelation," *Optics letters*, vol. 40, no. 23, pp. 5518–5521, 2015.

[14] B. Wang, K. Tao, X. Hu, W. Chen, Z. Wen, X. Liu, C. You, Z. Geng, X. Li, R. Liu, and D. Wu, "Intravascular optical coherence tomography utilizing a miniature piezoelectric-driven probe," *IEEE Transactions on Biomedical Engineering*, vol. 70, no. 12, pp. 3490–3500, 2023.

[15] M. J. Gora, M. J. Suter, G. J. Tearney, and X. Li, "Endoscopic optical coherence tomography: technologies and clinical applications," *Biomedical optics express*, vol. 8, no. 5, pp. 2405–2444, 2017.

[16] T. Mashimo and S. Izuhara, "Recent advances in micromotors," *IEEE Access*, vol. 8, pp. 213 489–213 501, 2020.

[17] T. Wang, C. Lancée, R. Beurskens, J. Meijer, B. Knapen, A. F. van der Steen, and G. van Soest, "Development of a high-speed synchronous micro motor and its application in intravascular imaging," *Sensors and Actuators A: Physical*, vol. 218, pp. 60–68, 2014.

[18] J. Wang, J. Xue, S. Yuan, J. Tan, S. Song, and M. Q.-H. Meng, "Kinematic modeling of magnetically-actuated robotic catheter in nonlinearly-coupled multi-field," *IEEE Robotics and Automation Letters*, vol. 6, no. 4, pp. 8189–8196, 2021.

[19] S. Song, S. Yuan, F. Zhang, J. Su, D. Ye, J. Wang, and M. Q.-H. Meng, "Integrated design and decoupled control of anchoring and drug release for wireless capsule robots," *IEEE/ASME Transactions on mechatronics*, vol. 27, no. 5, pp. 2897–2907, 2021.

[20] J. Tan, J. Xue, X. Yang, S. Yuan, W. Liu, H. Ren, S. Song, and J. Wang, "Model-free and uncalibrated visual-feedback control of magnetically-actuated flexible endoscopes," in *2022 IEEE/RSJ International Conference on Intelligent Robots and Systems (IROS)*. IEEE, 2022, pp. 5930–5936.

[21] S. Yuan, C. Xu, B. Cui, T. Zhang, B. Liang, W. Yuan, and H. Ren, "Motor-free telerobotic endomicroscopy for steerable and programmable imaging in complex curved and localized areas," *Nature Communications*, vol. 15, no. 1, p. 7680, 2024.

[22] M. Adaramola, *Wind turbine technology: Principles and design*. CRC Press, 2014.

[23] A. Petersson, *Analysis, modeling and control of doubly-fed induction generators for wind turbines*. Chalmers Tekniska Hogskola (Sweden), 2005.

[24] R. E. Froude, "On the part played in propulsion by differences of fluid pressure," *Trans. Inst. Naval Architects*, vol. 30, p. 390, 1889.

[25] A. Betz, "Das maximum der theoretisch möglichen ausnützung des windes durch windmotoren," *Zeitschrift für das gesamte Turbinenwesen*, 1920.

[26] M. O. Hansen, *Aerodynamics of wind turbines*. Routledge, 2015.

[27] J. N. Sørensen, "Aerodynamic aspects of wind energy conversion," *Annual Review of Fluid Mechanics*, vol. 43, pp. 427–448, 2011.

[28] C. Xu, X. Guan, S. A. Abbasi, N. Xia, T. Ngai, L. Zhang, H.-P. Ho, S. H. C. Ng, and W. Yuan, "Liquid-shaped microlens for scalable production of ultrahigh-resolution optical coherence tomography microendoscope," *Communications Engineering*, vol. 3, no. 1, p. 1, 2024.

[29] T. Zhang, S. Yuan, C. Xu, P. Liu, H.-C. Chang, S. H. C. Ng, H. Ren, and W. Yuan, "Pneumaoct: Pneumatic optical coherence tomography endoscopy for targeted distortion-free imaging in tortuous and narrow internal lumens," *Science Advances*, vol. 10, no. 35, p. eadp3145, 2024.